

1       **A Raman lidar to measure water vapor in the atmospheric boundary layer**  
2  
3

4       Martin Froidevaux<sup>1</sup>, Chad W. Higgins<sup>\*2</sup>, Valentin Simeonov<sup>1</sup>, Pablo Ristori<sup>3</sup>, Eric  
5       Pardujak<sup>4</sup>, Ilya Serikov<sup>5</sup>, Ronald Calhoun<sup>6</sup>, Hubert van den bergh<sup>1</sup>, Marc B. Parlange<sup>1</sup>  
6

7                   1 School of Architecture, Civil and Environmental Engineering,  
8                   Ecole Polytechnique Fédérale de Lausanne (EPFL)  
9

10                   2 Department of Biological and Ecological Engineering,  
11                   Oregon State University, Corvallis  
12

13                   3 -CEILAP (CITEFA-CONICET) - Zufriategui – Argentina  
14

15                   4 Department of Mechanical Engineering  
16                   University of Utah, Salt Lake City  
17

18                   5 Max-Planck-Institut für Meteorologie  
19                   Hamburg  
20

21                   6 Arizona State University, Tempe  
22  
23  
24  
25  
26  
27  
28

29       \*Corresponding author address: Chad Higgins, 116 Gilmore Hall, Corvallis, OR  
30       97331

31       Keywords: Atmospheric Boundary Layer, Raman Lidar, Water Vapor

## Abstract

1  
2  
3 A new multi-telescope scanning Raman lidar designed to measure the water vapor  
4 mixing ratio for a complete diurnal cycle with high raw spatial (1.25 m) and temporal  
5 (1 s) resolutions is presented. The high resolution allows detailed measurements of the  
6 lower atmosphere and offers new opportunities for boundary layer research,  
7 atmospheric profiling and visualization. This lidar utilizes a multi-telescope design  
8 that provides for an operational range with a nearly constant signal-to-noise ratio,  
9 which allows for statistical investigations of atmospheric turbulence. This new  
10 generation ground-based water vapor Raman lidar is described, and first observations  
11 from the Turbulent Atmospheric Boundary Layer Experiment (TABLE) are  
12 presented. Direct comparison with in-situ point measurements obtained during the  
13 field campaign demonstrate the ability of the lidar to reliably measure the water vapor  
14 mixing ratio. Horizontal measurements taken with time are used to determine the  
15 geometric characteristics of coherent structures. Vertical scans are used to visualize  
16 nocturnal jet features, layered structures within a stably stratified atmosphere and the  
17 internal boundary layer structure over a lake.  
18

## 1       **1. Introduction**

2       The development of new instrumentation to probe the spatial characteristics of the  
3       atmospheric boundary layer (ABL) is paramount to improving our understanding of  
4       land-atmosphere exchange over complex terrain (Parlange, Eichinger et al. 1995;  
5       Eichinger, Cooper et al. 2006). The variability of the earth's surface with respect to  
6       topography, surface roughness, soil moisture distribution, and land use impact the  
7       various scales of motion in the turbulent ABL, and the resulting local transport of  
8       heat, water vapor, and momentum. While fast response point sensors have become  
9       standard in the micrometeorological community due to their relatively reliable and  
10      robust operation (Lenshow 1986), measurements of the spatial variability of  
11      atmospheric turbulence over field scales, on the order of 500 m, has remained less  
12      well developed. Arrays of sonic anemometers have been used to obtain spatially  
13      resolved measurements of turbulence quantities with typical array sizes limited to  
14      10's of meters (Schmid 1994; Tong, Wyngaard et al. 1999; Porte-Agel, Meneveau et  
15      al. 2000; Kleissl, Parlange et al. 2004; Higgins, Meneveau et al. 2009; Kelly,  
16      Wyngaard et al. 2009; Bou-Zeid, Higgins et al. 2010). These spatial data sets have  
17      proven invaluable for a priori understanding subgrid scale physics for Large-Eddy  
18      Simulation (Lesieur, Begou et al.), but lack the full range of spatial scales resolved by  
19      LES.

20      High resolution numerical approaches such as LES have been used to simulate the  
21      interactions of the land surface with the atmosphere over complex terrain (Shaw and  
22      Schumann 1992; Patton, Shaw et al. 1998; Albertson and Parlange 1999; Lesieur,  
23      Begou et al. 2003; Watanabe 2004; Yang, Raupach et al. 2006; Dupont and Brunet  
24      2009). These simulations require land surface boundary and atmospheric initial  
25      conditions (Albertson, Kustas et al. 2001), as well as new means of validation. Thus,

1 there remains an obvious requirement for measurement tools that can temporally and  
2 spatially resolve the multiple atmospheric scales responsible for the transport of heat,  
3 water vapor and momentum at the land-atmosphere interface.

4 The use of range resolved remote sensors (e.g. sodar, lidar, radar) over the past  
5 decades in atmospheric research has had a significant impact on our knowledge of the  
6 boundary layer, e.g. (Neff 1978; Cooper, Eichinger et al. 1992; Liu and Bromwich  
7 1993; Senff, Bosenberg et al. 1994; Angevine, Grimsdell et al. 1998; Cohn, Mayor et  
8 al. 1998; Devara 1998; Fochesatto, Drobinski et al. 2001; Kollias, Albrecht et al.  
9 2001). These devices have been used to gain tremendous insight into various  
10 processes in the atmospheric boundary layer (e.g. entrainment, dispersion, etc.) as  
11 well as particular quantities in the atmospheric boundary layer that have been  
12 traditionally difficult to measure (e.g. boundary layer heights, inversion depths, etc.)  
13 (Wilczak, Gossard et al. 1996). However, these techniques are still limited to  
14 relatively large spatial and temporal resolutions. Two historically competing lidar  
15 technologies for remote sensing of water vapor are the DIAL (differential absorption  
16 of light) and Raman lidars (Grant 1991). DIAL lidars utilize a combination of particle  
17 and molecule scatter, while Raman lidars operate on a principle based solely on  
18 scatter from molecules (Wilczak, Gossard et al. 1996). The advantages and  
19 disadvantages of the techniques have been reviewed by (Grant 1991).

20 The Raman lidar approach to measure water vapor in the atmosphere was initially  
21 proposed in the late 1960s (Leonard 1967; Cooney 1968), but its development was  
22 limited due technical difficulties such as unstable laser sources, inadequate data  
23 acquisition systems, and eye safety restrictions. The renewed interest in the Raman  
24 lidar technique for water vapor measurements was kindled by the results presented in  
25 (Melfi and Whiteman 1985; Vaughan, Wareing et al. 1988). The main advantage of

1 the Raman lidar approach, compared to other approaches, is that the laser source does  
2 not have to be tuned to a specific water vapor absorption line (Grant 1991).  
3 Additionally, Raman lidar allows for the high spatial and temporal resolution that is  
4 necessary to study the turbulent atmosphere boundary layer dynamics. The Raman  
5 lidar technique is now well established as an advanced research tool in the  
6 atmospheric sciences (Renaut, Pourny et al. 1980; Koch, Dorian et al. 1991;  
7 Whiteman, Melfi et al. 1992; Pinzon, Puente et al. 1995; Goldsmith, Blair et al. 1998;  
8 Turner, Ferrare et al. 2002; Tratt, Whiteman et al. 2005; Whiteman, Demoz et al.  
9 2006; Eichinger and Cooper 2007; Hua, Liu et al. 2007). Limitations such as low  
10 spatial and temporal resolution, day-time operation, and signal attenuation with range  
11 ( $1/r^2$  where  $r$  is distance from the laser source) have led to the limited use of Raman  
12 lidars in micrometeorology. Solutions for day-time operation have been proposed by  
13 (Renaut, Pourny et al. 1980; Goldsmith, Blair et al. 1998) and have been used to guide  
14 our design.

15 In this paper we present a new ground-based scanning Raman lidar designed to  
16 measure the water vapor mixing ratio at high spatial (1.25m) and temporal (1s)  
17 resolution over a range of up to 500 meters at near constant signal-to-noise ratio  
18 (SNR). A description of the field deployment, validation of the instrument, and first  
19 observations are presented. We show that the Raman lidar can be used to identify and  
20 characterize features of the atmospheric boundary layer that have traditionally been  
21 difficult to measure including: advected coherent structures, the impact of the  
22 nocturnal jet, layering resulting from stable atmosphere stratification, and internal  
23 boundary layer formation at land surface transitions.

24

## 1        **2. EPFL high resolution Raman lidar**

2        The EPFL (Ecole Polytechnique Fédérale de Lausanne) instrument is a solar-  
3 blind, scanning Raman lidar. The lidar was designed to measure water vapor mixing  
4 ratio during the day and night with raw spatial and time resolutions of 1.25 m and 1 s  
5 respectively. The primary design challenges arise due to the demanding temporal and  
6 spatial resolution requirements with almost constant accuracy within the range of 15-  
7 500 m. The novel, multi-telescope design of the lidar, (see Appendix for more details)  
8 allows for water vapor profiling with almost constant measurement error over the  
9 whole operational range. By contrast, the measurement error of conventional lidars  
10 increases quadratically with the measurement range. Daytime operation is achieved  
11 by using UV wavelengths shorter than 300 nm which fall within the ‘solar blind’  
12 region of the electromagnetic spectra, thus ensuring that daylight has a minimal effect  
13 on the measurements. Azimuthal and elevation scanning with a resolution of 1° and  
14 scanning speeds up to 6°/min allow for observation of a hemisphere centered on the  
15 laser light source.

16        Some of the technical advances made to overcome these challenges are discussed  
17 in the detailed description given in the Appendix.

18

19

## 20        **3. TABLE-08**

21        The TABLE-08 (Turbulent Atmospheric Boundary Layer Experiment) was  
22 carried out during the month of August 2008 in Seedorf (FR/Switzerland) around and  
23 above a small lake (46.78444° N, 7.04083° E). The objective of the TABLE-08 field  
24 experiment was to validate the EPFL high resolution Raman lidar and to study the  
25 effects of the lake on the local microclimate.

1 The site is located on the Swiss plateau at a drained peat bog that has been  
2 converted into productive agriculture fields. The site is surrounded by hills that extend  
3 ~120 m above the valley floor toward the North and South. A lake, in the center on  
4 this small valley, is fed mainly by ground water contributions. The lake is about 400  
5 m wide and is surrounded by tall grass, creating a rough transition between the water  
6 and the surrounding agriculture fields. Figure 1 is a photograph of the lake looking  
7 toward the West showing the instrumental setup and the state of vegetation during the  
8 field campaign. A profile of the terrain running along the lidar beam path is sketched  
9 at the bottom of the figure. Horizontal lidar measurements were taken with a small  
10 inclination of 1.5 degrees to ensure eye safety. With this configuration, the laser beam  
11 was at heights of 2.5, 4.34 and 7.07 m above ground respectively at towers 2, 3 and 4.  
12 Thus, the lidar beam passed within ~30 cm of the sensors mounted on each tower  
13 where the water vapor mixing ratio was measured with two different techniques:  
14 LICOR LI7500 fast response infrared gas analyzer and calibrated slow response  
15 Rotronic XB temperature relative humidity sensors. Tower 2 was also instrumented to  
16 measure the surface energy budget, including fully resolved radiation balance, soil  
17 heat flux, and sensible/latent heat flux measurements. A sodar/RASS system,  
18 providing vertical profiles of wind speed, wind direction and virtual temperature, was  
19 installed close the lake edge. A tethered balloon equipped with a Meteolabor “Snow-  
20 White” chilled mirror dewpoint hygrometer to measure temperature and humidity was  
21 used for atmospheric profiling from ground level to 150 m (height limited by civil and  
22 military aviation security). The lake surface temperature was also monitored with  
23 HOBO TidBit v2 thermometers attached to the bottom of Styrofoam flotation devices  
24 at three locations, aligned under the laser beam. The complete description of the

1 TABLE-08 instrumental setup with measured variables, sensor types, sampling rates  
2 and accuracies is summarized in Table 1.

3

### 4 ***3.1 Verifying the lidar performance***

5 Data with a signal-to-noise ratio less than 5 were rejected. Also known as the  
6 Rose criterion, it is the SNR needed to distinguish image features with 100% certainty  
7 (Bushberg 2002). A sensitivity analysis was performed to determine the effect of  
8 temporal averaging on the maximum range of the instrument (defined as the range  
9 where the SNR drops below 5). As expected, longer averaging times resulted in a  
10 greater effective range of the instrument; however, the range reached an absolute  
11 maximum at 1200 m where additional averaging no longer extended the range.  
12 The proximity of the horizontal staring position of the laser beam to the tower's  
13 sensors allowed for assessment of the lidar calibration at three different points.  
14 Ideally, a single calibration should apply if the multi-telescopes lidar design is  
15 suitable for accurate measurements of water vapor over the entire measurement range.  
16 Two minute averages of the water vapor mixing ratio from the towers were compared  
17 to the ratio of water vapor to nitrogen Raman scattering obtained from the lidar over  
18 the same time interval. The lidar signal was then averaged over three bins,  
19 corresponding to 3.75 m. To obtain a proper calibration, a wide range of absolute  
20 water vapor mixing ratio values are needed; for this purpose, 18 hours of  
21 measurements over three days are used (20, 22, and 25 August 2008) with mixing  
22 ratios ranging from 7.5 to 11 grams of water vapor per kilogram of dry air. The  
23 calibration constants are computed for the three different ranges, 60, 135 and 513  
24 meters, each tower independently or the three combined (



1 Figure 2). The maximum deviation for the range independent calibration, computed  
 2 with a least squared linear regression, was ~5% with the largest error at tower 4. The  
 3 best calibration function considering the three towers simultaneously is given by:

$$4 \quad MR_{lidar} = 1.888 \frac{S_{H_2O}}{S_{N_2}} + 1.993 \quad (1)$$

5 In Eq. (1),  $MR_{Lidar}$  is the lidar retrieved water vapor mixing ratio in  $g/kg_{dry}$ ,  $S_{H_2O}$  and  
 6  $S_{N_2}$  are the baseline corrected rotational-vibrational Raman signals from water vapor  
 7 and nitrogen, respectively. The comparison is excellent with  $R^2$  values of 0.946, 0.862  
 8 and 0.726 at the three different ranges from the lidar and for 2 min averaging of the  
 9 signal. The measurement accuracies, defined as the standard deviation of the  
 10 difference between both types of measurements are 0.16, 0.23 and 0.32  $g/kg_{dry air}$  for  
 11 towers 2, 3 and 4, respectively. At ambient temperature, a shift of 0.3  $g/kg_{dry air}$  in the  
 12 mixing ratio corresponds to approximately 1.7 % relative humidity. A comparison of  
 13 variances and spectra given by the lidar and LICOR7500 was also performed and  
 14 presented in (Higgins, Froidevaux et al. 2012).

### 15 **3.2 Horizontal observations**

16 Valuable insight into the flow structures passing over the lake can be obtained  
 17 when the lidar is pointed horizontally at a fixed height and the mixing ratio is  
 18 measured along the beam in time. Figures 3 and 4 show a contour plot from this type  
 19 of experiment. Numerous diagonal stripes are observed in the time-space-mixing ratio  
 20 graphs. Such water vapor signatures are visible during most daytime horizontal  
 21 sounding periods at the TABLE-08 site. Two measurement periods where horizontal  
 22 measurements are taken are shown below; one with the wind blowing from the lidar  
 23 to the lake (Figure 3), and a second with the wind blowing across the lake toward the  
 24 lidar (Figure 4). Note that in both figures, the air above the land surface has a higher

1 water vapor mixing ratio. This is expected in the daytime as the land surface is much  
2 warmer than the lake surface and the land surface supports an actively transpiring  
3 crop of clover. Also in both figures, persistent flow features are visible independent  
4 of wind direction, and support the idea that such humidity patterns are not specific to  
5 certain surface roughness properties (e.g., corn field, harvested weeds, fallows,  
6 clovers and trees) but are more universal.

7 The persistent flow features were first analyzed by correlating the observed  
8 velocity vectors with the advected humidity structures in an attempt to tease out the  
9 underlying physical mechanisms. In such a case, relationships between the humidity  
10 structures observed with the lidar, and the wind vector components measured by  
11 ultrasonic anemometers are expected. Furthermore, patterns in the velocity signal are  
12 expected to advect across the experimental transect with the humid structures. A time  
13 series of the lidar humidity data is presented alongside the fluctuating velocity  
14 components at each tower in Figure 5. Regions with a  $SNR < 5$  are displayed in black.  
15 The relationship between the lidar data and these wind patterns is not obvious.  
16 Ejection and sweep events do not correspond exactly in time to higher values of  
17 mixing ratio lidar measurements, and there is no clear pattern that is advected from  
18 one tower to another. For example, the two largest wind events at tower 3 (135 m in  
19 the time-space lidar plot), correspond to a high humidity event (13:09) and a low  
20 humidity event (13:23) respectively.

21 Since no clear pattern emerged from the analysis of wind vector components, A  
22 geometric approach was adopted. With this approach, each coherent humidity  
23 structure is identified and analyzed according to the approach summarized in Figure  
24 6(a). In Figure 6(a), a plan view of a portion of the beam is sketched. The blue box  
25 represents a coherent structure, which enters the beam at a certain time ( $t_3$ ) and range

1 (r3). The wind advects this structure up to a point where it completely crosses the  
2 lidar beam (central light blue box), and until it finally leaves the beam (last light blue  
3 box). The extent of an individual structure along the beam (r1 and r2) and the  
4 propagation time (t3 and t4) can be determined directly from the lidar data. Combining  
5 this information with the wind speed, and the angle of the wind with respect to the  
6 laser beam orientation, the span-wise dimension of this coherent signature  $W$  is  
7 retrieved. The stream-wise dimension  $L$  is obtained by taking the distance along the  
8 beam when the structure enters and leaves the sounding beam (r3 and r4). This simple  
9 method is applied to the calibration days (20, 22, and 25 August 2008), corresponding  
10 to 18 hours of measurements, where 137 structures have been quantified. Histograms  
11 of the stream-wise and span-wise extent of the coherent structures determined from  
12 the above analysis are presented in Figure 6(b) and Figure 6(c) respectively. The  
13 major result of this analysis is that the stream-wise extent of these structures, in the  
14 direction of the wind, is approximately two times larger than the span-wise extent.  
15 Thus, these coherent structures could be imagined as elongated patterns of moisture,  
16 which are consistent with nested packets of hairpin vortices. The existence of self-  
17 organizing vortices in the mixed layer is still subject to study in the atmospheric  
18 boundary layer community. (Finnigan 2000; Garai and Kleissl 2011). Numerical  
19 simulations have been used to reproduce and understand such structures, with DNS  
20 (i.e. (Jeong, Hussain et al. 1997; Waleffe 1997; Schneider, Farge et al. 2005)) or LES  
21 (i.e. (Shaw and Schumann 1992; Patton, Shaw et al. 1998; Lesieur, Begou et al. 2003;  
22 Watanabe 2004; Yang, Raupach et al. 2006; Dupont and Brunet 2009)). Observations  
23 of such structures have been obtained in wind tunnel facilities (Brunet, Finnigan et al.  
24 1994; Judd, Raupach et al. 1996; Nishi, Kikugawa et al. 1999; Finnigan and Shaw  
25 2000). Previous studies of vortex organization in the turbulent boundary layer with

1 Particle Image Velocimetry (PIV), have shown that hairpin vortex signatures populate  
2 the boundary layer abundantly (Adrian, Meinhart et al. 2000), and the conceptual  
3 representation they give seems to be the best match to the phenomena observed with  
4 the lidar. Such bended tubes with heads up and the tails close to the ground induce  
5 low speed fluid cores from near the surface. This could explain why coherent  
6 signatures of humidity have been measured at different heights over the entire lidar  
7 measurements range and over different roughness transitions. Still, one may ask the  
8 question, is the humidity observed in the field consistent with an organized nested  
9 packet of hairpin vortices? One hypothesis is that, due to its smaller density, water  
10 vapor is taken from the ground and concentrated in the induced low speed fluid core  
11 of the hairpin packet. To our knowledge, it is the first time that such complete  
12 structures have been measured systematically in the space-time domain with water  
13 vapor Raman lidar at field scales.

### 14 ***3.3 Vertical scans***

15 The scanning ability of the EPFL Raman lidar allows for different visualizations  
16 of the atmosphere compared to a static orientation. Three vertical scans are presented  
17 below, which demonstrate three types of atmospheric boundary layer phenomena: a  
18 nocturnal jet, a multi-layered stable atmosphere, and an internal boundary layer that  
19 develops above Seedorf lake. Each colored contour plot represents the distance-  
20 altitude-mixing ratio concentration measured with Raman lidar during one scan. The  
21 experimental setup with the wind direction and wind speed measured at 2.5 m above  
22 ground are sketched at the top of each of the panels in Figures 6-8.

#### 23 ***Nocturnal jet***

24 This lidar vertical downward scan (Figure 7), taken during the TABLE-08 field  
25 campaign was recorded from 02:03 to 02:20 CET on the 30<sup>th</sup> of August 2008. The

1 small black dots at the bottom part of the scan are inconsistent values due to fog  
2 scattering. Two profiles of horizontal wind speed, wind direction, vertical wind speed  
3 and virtual potential temperature measured by the sodar/RASS during the scan  
4 interval time are shown on the right. The vertical lidar scan shows a less humid layer  
5 of air between 200 and 350 m, which corresponds to a nocturnal jet with a maximum  
6 speed of 7 m/s centered at 280 m. At low altitude, a strong change of wind direction is  
7 visible in the sodar data and is related to the lowest visible humidity layer on the lidar  
8 scan, at about 40 m above ground. The virtual potential temperature profile from the  
9 RASS, does not completely match the water vapor layers.

### 10 ***Multilayered stable atmosphere***

11 Figure 8 shows an example of a stably stratified and layered atmosphere. It is a  
12 downward vertical scan, acquired between 21:10 and 21:31 CET on the 29<sup>th</sup> of  
13 August 2008. Three mean vertical profiles are extracted from this scan and presented  
14 in the right panel of Figure 8. The blue line is a vertical profile taken above the grass  
15 field upwind of the lake, the green line corresponds to the middle part of the  
16 experiment above the lake and the red line was obtained just downwind of the lake.  
17 These extracted profiles illustrate the multi-scale behavior a stably stratified  
18 atmosphere above the lake. There are three main layers, surrounded by smaller  
19 secondary layers, which are in turn surrounded by even smaller tertiary layers. This  
20 layering occurred during one of the most stable episodes observed over the land  
21 surface with  $z/L = 0.91$  measured at Tower 2, where  $L$  is the well-known Obukhov  
22 length. In the same vertical lidar scan, the internal boundary layer of the lake, trapped  
23 inside the first layer, can be also seen. This observation is partially confirmed by the  
24 shape of the first 100 m from the three vertical extracted profiles (Figure ). The wind  
25 at 2.5 m above ground, measured with the cup and vane anemometer, is southeasterly

1 blowing across the lake. Thus, the first extracted profile should not be influenced by  
2 the presence of the lake. The second profile was taken above the lake and exhibits  
3 higher mixing ratios; likely due to the lake water vapor transfer. Finally the third  
4 profile, taken downwind, shows a similar mixing ratio value at the ground as the one  
5 taken before the lake. This last profile has a peak at ~70 m, corresponding to the lake's  
6 water vapor internal boundary layer extent. The presence of an internal boundary  
7 layer is expected at this time, as the lake surface temperature was higher than the  
8 surrounding land surface and air temperature.

### 9 *Lake internal boundary layer*

10 The behavior of the development of internal boundary layers (IBLs) in the  
11 atmosphere associated with the horizontal advection of air across discontinuities is a  
12 subject of great interest and one in which there is still a great deal of scientific  
13 uncertainty (Garratt 1990). The EPFL Raman lidar provides a tool to investigate the  
14 spatial and temporal details of humidity with IBLs. Figure 9 shows the lowest portion  
15 of a 90° vertical lidar scan looking downwind from the lidar, measured from 18:31 to  
16 18:53 CET on the 28<sup>th</sup> of August 2008. The time required to scan the lower region  
17 near the ground, which included the IBL, was approximately 6 min. Simultaneous  
18 wind and temperature profile measurements from the sodar/RASS are presented  
19 below the lidar scan. As illustrated by the virtual potential temperature profiles shown  
20 in Figure 9, the atmosphere during the scan was stable above ~75 m. In the figure, the  
21 lake is located between 140 and 480 m. In the presented case, the discontinuities of  
22 the land surface are: roughness changes (from agriculture field to water surface with  
23 tall grass along the edge of the lake), temperature changes (from vegetated soil to  
24 water) and of course humidity (from land surface to open water). Different  
25 mathematical descriptions have been proposed in the literature for the different types

1 of internal boundary layers as a function of the surface propriety changes. For  
 2 example, (Sutton 1934) developed an analytical approach to describe the IBL  
 3 development over a step change in near-surface humidity, from relatively dry to wet  
 4 surfaces. His theory was further expanded by (Frost 1946) and is discussed in detail  
 5 by (Brutsaert 1982). The key assumptions are steady horizontal wind and negligible  
 6 variation of mean velocities in the vertical and lateral directions leading to a balance  
 7 between horizontal advection and divergence of the vertical turbulent flux of water  
 8 vapor in the mean water vapor budget. This leads to the following equation, which  
 9 describes the thickness of the internal boundary layer of the water vapor as a function  
 10 of along-wind fetch  $x$ :

$$11 \quad \delta_v = cx^{(2+m-n)^{-1}}. \quad (2)$$

12 Here,  $m = 1/7$  and  $n = 1-m$  for neutral stability flows,  $c = 1.82$ , and  $x$  is the direction  
 13 along the land surface aligned with the mean wind and  $x = 0$  is the dry to wet  
 14 interface position. Equation 2 is plotted on Figure 9, and shows excellent agreement  
 15 with the observed internal boundary layer. It is interesting to note that this internal  
 16 boundary layer was captured at about 18:50, and appeared right after the change of  
 17 stability regime over the land, from unstable to stable.

#### 18 **4. Conclusion**

19 The objectives of this study were to validate the multi-telescope design of the  
 20 EPFL Raman lidar and to evaluate the ability of this instrument to measure water  
 21 vapor mixing ratio and land-atmosphere exchange. The lidar-point sensor comparison  
 22 performed during the TABLE-08 field campaign demonstrates the ability of the lidar  
 23 to accurately measure the water vapor mixing ratio, and validates its multi-telescope  
 24 design. The accuracy of the water vapor mixing ratio is better than  $0.32 \text{ g kg}^{-1}$  of dry

1 air, when compared signals averaged over 2 minutes and a height increment of 3.75 m  
2 along the laser beam. The horizontal measurements of water vapor coherent  
3 structures, their analysis and the corresponding eddy covariance data allow us to  
4 claim that such patterns are consistent with the expected geometry of the cores of  
5 nested packets of hairpin vortices. It is the first time that such structures have been  
6 measured with a Raman lidar.

7       The scanning capability and the high temporal and spatial resolution of this  
8 Raman lidar offer a broad range of potential applications. The vertical scans give  
9 information about the extent of layers and boundary layer structures. Evidence of  
10 strong relationships between low-level jets and the water vapor distribution in the air  
11 have been observed. The multi-scale layering of the stable boundary layer has been  
12 described. The humid internal boundary layer over the lake has been also measured  
13 successfully. This study demonstrates the ability of a state-of-the-art Raman lidar to  
14 measure land-atmosphere interactions and offers a promising new vision and  
15 understanding of the atmospheric boundary layer.

16

17



## APPENDIX A

**Water vapor Raman lidar**

A lidar (LIght Detection And Ranging) is a laser-based, optical instrument, which allows remote profiling of atmospheric parameters such as aerosol backscatter, humidity, temperature, gas concentration, wind speed and direction(Weitkamp 2005).

A lidar transmits short laser pulses into the atmosphere and detects and analyzes the backscattered light from the atmosphere. This backscattered light contains information on atmospheric properties. The range to a scattering volume is determined by measuring the time between the transmission of the laser pulse and the detection of the backscattered radiation. Since the length of the instantly probed air volume is proportional to the laser pulse duration, the latter determines the profile range resolution.

The power of the backscattered light  $P(r)$  is proportional to the transmitted laser power  $P_0$ , telescope surface area  $A$ , and instrumental efficiency  $\eta$  and depends on the backscatter coefficient  $\beta(r)$  and atmospheric transmission  $T(r)$  through the so called scattering lidar equation:

$$P(r) = P_0 \frac{A}{r^2} \ln \beta(r) T^2(r), \quad (\text{A.1})$$

where  $r$  is the along beam distance,  $l = c\tau/2$  is the spatial resolution (depth of the scattering volume),  $c$  is the speed of light, and  $\tau$  the laser pulse duration.

In the special case of inelastic light-matter interaction, known as Raman scattering, the backscatter coefficient is proportional to the number density of the scattering molecules. The scattered wavelength differs from the laser wavelength and is specific for each scattering compound. These properties of Raman scattering are used in Raman lidars for water vapor mixing ratio measurements. The water vapor

1 profile  $q(r)$  is derived from the ratio of water vapor  $P_{H_2O}(r)$  to nitrogen  $P_{N_2}(r)$  Raman  
 2 signals as:

$$3 \quad q(r) = k \frac{P_{H_2O}(r)T_{N_2}(r)}{P_{N_2}(r)T_{H_2O}(r)} \Gamma(r), \quad (\text{A.2})$$

4 where  $k$  is a calibration coefficient determined by comparison with a reference  
 5 instrument. The ratio  $T_{N_2}(r)/T_{H_2O}(r)$  accounts for the difference in the atmospheric  
 6 transmission at the water vapor and nitrogen Raman wavelengths due particle  
 7 scattering which can be neglected in under clear atmospheric conditions.  $\Gamma(r)$  is a  
 8 correction function for the difference in the atmospheric transmission due to  
 9 molecular scattering and absorption. At laser wavelengths longer than 320 nm, the  
 10 main contribution to  $\Gamma(R)$  is due to Rayleigh scattering by air molecules and can be  
 11 calculated precisely from pressure profiles. At shorter wavelengths the differences in  
 12 the ozone absorption have to be taken into account. The ozone correction can be  
 13 estimated from the average ozone concentration, measured independently (Eichinger,  
 14 Cooper et al. 1999) or by using an additional Raman signal (Renaut, Pourny et al.  
 15 1980).

16 The majority of the existing Raman lidars are built with the goal to cover the  
 17 largest possible part of the troposphere. Raman lidars allow measurements up to the  
 18 stratosphere during the nighttime and up to the mid troposphere during the day.  
 19 Typical spatial resolutions for such systems are from tens of meters, to hundreds of  
 20 meters. The time resolution could be from minutes, close to the lidar, to hours at  
 21 longer distances see (Renaut, Pourny et al. 1980; Koch, Dorian et al. 1991; Whiteman,  
 22 Melfi et al. 1992; Pinzon, Puente et al. 1995; Goldsmith, Blair et al. 1998; Turner,  
 23 Ferrare et al. 2002; Tratt, Whiteman et al. 2005; Whiteman, Demoz et al. 2006;  
 24 Eichinger and Cooper 2007; Hua, Liu et al. 2007). The only lidar with high spatial

1 and temporal resolution, designed for short measurement distances, apart from the  
2 described here EPFL system, is the lidar described in (Eichinger, Cooper et al. 1999;  
3 Eichinger, Cooper et al. 2006).

4

### 5 **EPFL Raman lidar**

6 Since solar background in the visible spectrum is much greater than any  
7 Raman scattering, the EPFL lidar operates in the UV spectral band, known as the  
8 “solar-blind” region (wavelengths shorter than 300 nm), where nearly all solar  
9 radiation is absorbed by stratospheric ozone (Renaut, Pourny et al. 1980). Therefore,  
10 the lidar transmitter uses a quadrupled Nd:YAG laser, emitting 40 mJ pulses at 266  
11 nm with pulse duration of 4 ns and repetition rate of 100 Hz.

12

13 A novel “multi-telescope” array, designed to reduce the native high dynamic  
14 range of the lidar signals caused by the inherent  $1/r^2$  dependence (see Eq. A1 ), is used  
15 in the lidar receiver. The array consists of four parabolic mirrors with diameters of 10,  
16 20, 20, and 30 cm. The signals from the individual mirrors are summed optically to  
17 form a composite signal. The telescope sizes and their orientation with respect to the  
18 laser beam have been selected so that the intensity variation due to the range  
19 dependence of the composite signal is lower than 60% from 50 to 500 meters as  
20 shown in Figure A.1 (Ristori, Froidevaux et al. 2005; Serikov, Ristori et al. 2006;  
21 Ristori 2007). The small dynamic range of the composite signal yields nearly constant  
22 statistical error with constant temporal and spatial resolution over the entire  
23 operational range of the lidar while also helping to minimize the errors caused in the  
24 analog-to-digital conversion of the signals.

25

1           To simplify the optical scheme used for summing, the light from each  
2 telescope is delivered by optical fiber to the spectral unit used to separate the  
3 individual Raman signals. Dichroic beam-splitters, installed in front of each fiber,  
4 reflect light with a wavelength shorter than 274 nm, thus preventing systematic errors  
5 due to fluorescence in the optical fibers caused by the strong backscatter at the laser  
6 wavelength. This reflected short-wavelength radiation, contains pure Rotational lines  
7 of nitrogen and oxygen, and will be used for temperature measurements, now in  
8 development. The final wavelength separation of water, nitrogen, and oxygen Raman  
9 signals is performed by a prism- based polychromator. The oxygen channel is used to  
10 correct for the difference in the atmospheric transmission caused by tropospheric  
11 ozone at water vapor and nitrogen wavelengths (see Eq. A.2). The optical signals are  
12 detected in analog mode by photomultiplier tubes and acquired by eight channel 14  
13 bit, 120 MHz ADC.

14  
15           To allow for the observation of a wide range of ABL phenomena, the lidar has  
16 full-hemisphere scanning abilities. The elevation scanning is performed by rotating  
17 the telescope array around a horizontal axis. The laser beam is delivered along this  
18 axis by a set of mirrors and sent into the atmosphere coaxially aligned with the axis of  
19 the 10 cm telescope. The azimuthal scanning is carried out by rotating the whole lidar  
20 around a vertical axis (Figure A.2). Further details on the operational principles of the  
21 lidar can be found in (Froidevaux 2010).

## 1 **References**

2

3 Adrian, R. J., C. D. Meinhart, et al. (2000). "Vortex organization in the outer region  
4 of the turbulent boundary layer." Journal of Fluid Mechanics **422**: 1-54.

5 Albertson, J. D., W. P. Kustas, et al. (2001). "Large-eddy simulation over  
6 heterogeneous terrain with remotely sensed land surface conditions." Water  
7 Resources Research **37**(7): 1939-1953.

8 Albertson, J. D. and M. B. Parlange (1999). "Natural integration of scalar fluxes from  
9 complex terrain." Advances in Water Resources **23**(3): 293-252.

10 Angevine, W. M., A. W. Grimmsdell, et al. (1998). "Entrainment results from the  
11 Flatland boundary layer experiments." Journal of Geophysical Research-  
12 Atmospheres **103**(D12): 13689-13701.

13 Bou-Zeid, E., C. Higgins, et al. (2010). "Field study of the dynamics and modelling of  
14 subgrid-scale turbulence in a stable atmospheric surface layer over a glacier."  
15 Journal of Fluid Mechanics **665**: 480-515.

16 Brunet, Y., J. J. Finnigan, et al. (1994). "A wind-tunnel study of air-flow in waving  
17 wheat - single-point velocity statistics." Boundary-Layer Meteorology **70**(1-  
18 2): 95-132.

19 Brutsaert, W. (1982). Evaporation into the atmosphere. Theory, History and  
20 Applications, Reidel.

21 Bushberg, J. T. (2002). The Essential Physics of Medical Imaging, Lippincott  
22 Williams & Wilkins.

23 Cohn, S. A., S. D. Mayor, et al. (1998). "The lidars in flat terrain (LIFT) experiment."  
24 Bulletin of the American Meteorological Society **79**(7): 1329-1343.

25 Cooney, J. A. (1968). "Measurements on the Raman component of laser atmospheric  
26 backscatter." Appl. Phys. Lett. **12**(2): 40-42.

27 Cooper, D. I., W. E. Eichinger, et al. (1992). "Spatial variability of water-vapor  
28 turbulent transfer within the boundary-layer." Boundary-Layer Meteorology  
29 **61**(4): 389-405.

30 Devara, P. C. S. (1998). "Remote sensing of atmospheric aerosols from active and  
31 passive optical techniques." International Journal of Remote Sensing **19**(17):  
32 3271-3288.

- 1 Dupont, S. and Y. Brunet (2009). "Coherent structures in canopy edge flow: a large-  
2 eddy simulation study." Journal of Fluid Mechanics **630**: 93-128.
- 3 Eichinger, W. E. and D. I. Cooper (2007). "Using lidar remote sensing for spatially  
4 resolved measurements of evaporation and other meteorological parameters."  
5 Agronomy Journal **99**(1): 255-271.
- 6 Eichinger, W. E., D. I. Cooper, et al. (1999). "The development of a scanning raman  
7 water vapor lidar for boundary layer and tropospheric observations." Journal  
8 of Atmospheric and Oceanic Technology **16**(11): 1753-1766.
- 9 Eichinger, W. E., D. I. Cooper, et al. (2006). "Spatial and temporal variation in  
10 evapotranspiration using Raman lidar." Advances in Water Resources **29**(2):  
11 369-381.
- 12 Finnigan, J. (2000). "Turbulence in plant canopies." Annual Review of Fluid  
13 Mechanics **32**: 519-571.
- 14 Finnigan, J. J. and R. H. Shaw (2000). "A wind-tunnel study of airflow in waving  
15 wheat: An EOF analysis of the structure of the large-eddy motion." Boundary-  
16 Layer Meteorology **96**(1-2): 211-255.
- 17 Fochesatto, G. J., P. Drobinski, et al. (2001). "Evidence of dynamical coupling  
18 between the residual layer and the developing convective boundary layer."  
19 Boundary-Layer Meteorology **99**(3): 451-464.
- 20 Froidevaux, M. (2010). Land-Atmosphere Interactions Measured with Raman Lidar,  
21 École Polytechnique Fédérale de Lausanne.
- 22 Frost, R. (1946). "Turbulence and diffusion in the lower atmosphere." Proceedings of  
23 the Royal Society of London Series a-Mathematical and Physical Sciences  
24 **186**(1004): 20-35.
- 25 Garai, A. and J. Kleissl (2011). "Air and Surface Temperature Coupling in the  
26 Convective Atmospheric Boundary Layer." Journal of the Atmospheric  
27 Sciences **68**(12): 2945-2954.
- 28 Garratt, J. R. (1990). "THE INTERNAL BOUNDARY-LAYER - A REVIEW."  
29 Boundary-Layer Meteorology **50**(1-4): 171-203.
- 30 Goldsmith, J. E. M., F. H. Blair, et al. (1998). "Turn-key Raman lidar for profiling  
31 atmospheric water vapor, clouds, and aerosols." Applied Optics **37**(21): 4979-  
32 4990.
- 33 Grant, W. B. (1991). "differential absorption and Raman lidar for water vapor profile  
34 measurements: a review." Optical Engineering **30**(1): 40-48.

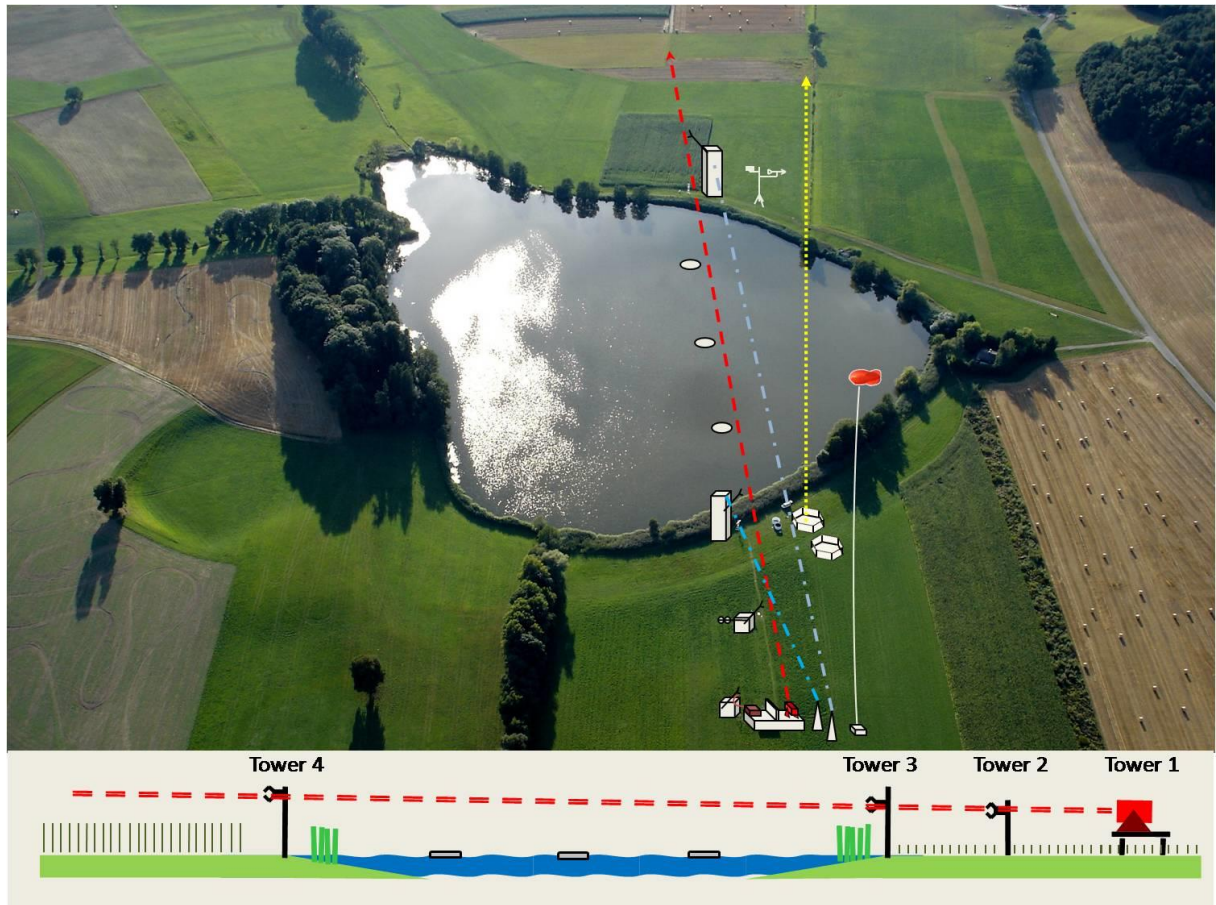
- 1 Grant, W. B. (1991). "DIFFERENTIAL ABSORPTION AND RAMAN LIDAR FOR  
2 WATER-VAPOR PROFILE MEASUREMENTS - A REVIEW." Optical  
3 Engineering **30**(1): 40-48.
- 4 Higgins, C., M. Froidevaux, et al. (2012). "The Effect of Scale on the Applicability of  
5 Taylor's Frozen Turbulence Hypothesis in the Atmospheric Boundary Layer  
6 has now been published in the following paginated issue of : Volume , Issue  
7 ( ), Page " Boundary-Layer Meteorology **143**(2): 379-391.
- 8 Higgins, C. W., C. Meneveau, et al. (2009). "Geometric Alignments of the Subgrid-  
9 Scale Force in the Atmospheric Boundary Layer." Boundary-Layer  
10 Meteorology **132**(1): 1-9.
- 11 Hua, D., J. Liu, et al. (2007). "Daytime temperature profiling of planetary boundary  
12 layer with ultraviolet rotational raman lidar." Japanese Journal of Applied  
13 Physics, Part 1: Regular Papers and Short Notes and Review Papers **46**(9 A):  
14 5849-5852.
- 15 Jeong, J., F. Hussain, et al. (1997). "Coherent structures near the wall in a turbulent  
16 channel flow." Journal of Fluid Mechanics **332**: 185-214.
- 17 Judd, M. J., M. R. Raupach, et al. (1996). "A wind tunnel study of turbulent flow  
18 around single and multiple windbreaks .1. Velocity fields." Boundary-Layer  
19 Meteorology **80**(1-2): 127-165.
- 20 Kelly, M., J. C. Wyngaard, et al. (2009). "Application of a Subfilter-Scale Flux Model  
21 over the Ocean Using OHATS Field Data." Journal of the Atmospheric  
22 Sciences **66**(10): 3217-3225.
- 23 Kleissl, J., M. B. Parlange, et al. (2004). "Field experimental study of dynamic  
24 Smagorinsky models in the atmospheric surface layer." Journal of the  
25 Atmospheric Sciences **61**(18): 2296-2307.
- 26 Koch, S. E., P. B. Dorian, et al. (1991). "Structure of an internal bore and dissipating  
27 gravity current as revealed by Raman lidar." Monthly Weather Review **119**(4):  
28 857-887.
- 29 Kollias, P., B. A. Albrecht, et al. (2001). "Radar observations of updrafts, downdrafts,  
30 and turbulence in fair-weather cumuli." Journal of the Atmospheric Sciences  
31 **58**(13): 1750-1766.
- 32 Lenshow, D. H., Ed. (1986). Probing the atmospheric boundary layer. Boston,  
33 American Meteorological Society.

- 1 Leonard, D. A. (1967). "Observation of Raman scattering from the atmosphere using  
2 a pulsed nitrogen ultraviolet laser." Nature **216**: 142-143.
- 3 Lesieur, M., P. Begou, et al. (2003). "Coherent-vortex dynamics in large-eddy  
4 simulations of turbulence." Journal of Turbulence **4**: 24.
- 5 Liu, Z. and D. H. Bromwich (1993). "Acoustic remote-sensing of planetary boundary-  
6 layer dynamics near Ross Island, Antarctica." Journal of Applied Meteorology  
7 **32**(12): 1867-1882.
- 8 Melfi, S. H. and D. N. Whiteman (1985). "Observation of lower-atmospheric moisture  
9 structure and its evolution using a Raman lidar." Bull. Am. Meteorol. **66**(10):  
10 1288-1292.
- 11 Neff, W. D. (1978). "Boundary-layer research at south-pole station using acoustic  
12 remote-sensing." Antarctic Journal of the United States **13**(4): 179-181.
- 13 Nishi, A., H. Kikugawa, et al. (1999). "Active control of turbulence for an  
14 atmospheric boundary layer model in a wind tunnel." Journal of Wind  
15 Engineering and Industrial Aerodynamics **83**: 409-419.
- 16 Parlange, M. B., W. E. Eichinger, et al. (1995). "Regional-scale evaporation and the  
17 atmospheric boundary-layer  
18 " Reviews of Geophysics **33**(1): 99-124.
- 19 Patton, E. G., R. H. Shaw, et al. (1998). "Large-eddy simulation of windbreak flow."  
20 Boundary-Layer Meteorology **87**(2): 275-306.
- 21 Pinzon, J. E., C. E. Puente, et al. (1995). "A multifractal analysis of lidar measured  
22 water vapour." Boundary-Layer Meteorology **76**(4): 323-347.
- 23 Porte-Agel, F., C. Meneveau, et al. (2000). "A scale-dependent dynamic model for  
24 large-eddy simulation: application to a neutral atmospheric boundary layer."  
25 Journal of Fluid Mechanics **415**: 261-284.
- 26 Renaut, D., J. C. Pourny, et al. (1980). "Day-time Raman-lidar measurements of water  
27 vapor." Optics Letters **5**(6): 233 -235.
- 28 Renaut, D., J. C. Pourny, et al. (1980). "DAYTIME RAMAN-LIDAR  
29 MEASUREMENTS OF WATER-VAPOR." Optics Letters **5**(6): 233-235.
- 30 Ristori, P. R. (2007). Development of a high spatial and temporal resolution Raman  
31 lidar for turbulent observations. PhD Thèse EPFL, no 3963 (2007), EPFL.
- 32 Ristori, P. R., M. Froidevaux, et al. (2005). Development of a temperature and water  
33 vapor Raman LIDAR for turbulent observations. Proceedings of SPIE - The  
34 International Society for Optical Engineering.



- 1 Schmid, H. P. (1994). "Source areas for scalars and scalar fluxes." Boundary-Layer  
2 Meteorology **67**(3): 293-318.
- 3 Schneider, K., M. Farge, et al. (2005). "Coherent vortex simulation of three-  
4 dimensional turbulent mixing layers using orthogonal wavelets." Journal of  
5 Fluid Mechanics **534**: 39-66.
- 6 Senff, C., J. Bosenberg, et al. (1994). "Measurements of water-vapor flux profiles in  
7 the convective boundary-layer with lidar and radar-RASS." Journal of  
8 Atmospheric and Oceanic Technology **11**(1): 85-93.
- 9 Serikov, I., P. Ristori, et al. (2006). Temperature and water vapor Raman lidar for  
10 observation of land-atmosphere interactions. 23rd International Laser Radar  
11 Conference, Nara, Japan.
- 12 Shaw, R. H. and U. Schumann (1992). "Large-eddy simulation of turbulent-flow  
13 above and within a forest." Boundary-Layer Meteorology **61**(1-2): 47-64.
- 14 Sutton, G. C. (1934). "Wind structure and evaporation in a turbulent atmosphere."  
15 Proceedings of the Royal Society of London Series a-Mathematical and  
16 Physical Sciences **146**(A858): 0701-0722.
- 17 Tong, C. N., J. C. Wyngaard, et al. (1999). "Experimental study of the subgrid-scale  
18 stresses in the atmospheric surface layer." Journal of the Atmospheric  
19 Sciences **56**(14): 2277-2292.
- 20 Tratt, D. M., D. N. Whiteman, et al. (2005). "Active Raman sounding of the earth's  
21 water vapor field " Spectrochimica Acta Part A **61**: 2335-2341.
- 22 Turner, D. D., R. A. Ferrare, et al. (2002). "Automated retrievals of water vapor and  
23 aerosol profiles from an operational raman lidar." Journal of Atmospheric and  
24 Oceanic Technology **19**(1): 37-50.
- 25 Vaughan, G., D. P. Wareing, et al. (1988). "Humidity measurements in the free  
26 troposphere using Raman backscatter." Quarterly Journal - Royal  
27 Meteorological Society **114**(484): 1471-1484.
- 28 Waleffe, F. (1997). "On a self-sustaining process in shear flows." Physics of Fluids  
29 **9**(4): 883-900.
- 30 Watanabe, T. (2004). "Large-eddy simulation of coherent turbulence structures  
31 associated with scalar ramps over plant canopies." Boundary-Layer  
32 Meteorology **112**(2): 307-341.
- 33 Weitkamp, C. (2005). Lidar: Range-resolved Optical Remote Sensing Of The  
34 Atmosphere, Springer Science+Business Media.

- 1 Whiteman, D. N., B. Demoz, et al. (2006). "Raman Lidar Measurements during the  
2 International H2O Project. Part II: Case Studies." J. Atm. Oceanic Technol.  
3 **23**(2): 170-183.
- 4 Whiteman, D. N., S. H. Melfi, et al. (1992). "Raman lidar system for the measurement  
5 of water vapor and aerosols in the Earth's atmosphere." Applied Optics **31**(16):  
6 3068-3082.
- 7 Wilczak, J. M., E. E. Gossard, et al. (1996). "Ground-based remote sensing of the  
8 atmospheric boundary layer: 25 years of progress." Boundary-Layer  
9 Meteorology **78**(3-4): 321-349.
- 10 Yang, B., M. R. Raupach, et al. (2006). "Large-eddy simulation of turbulent flow  
11 across a forest edge. Part I: Flow statistics." Boundary-Layer Meteorology  
12 **120**(3): 377-412.
- 13  
14  
15  
16

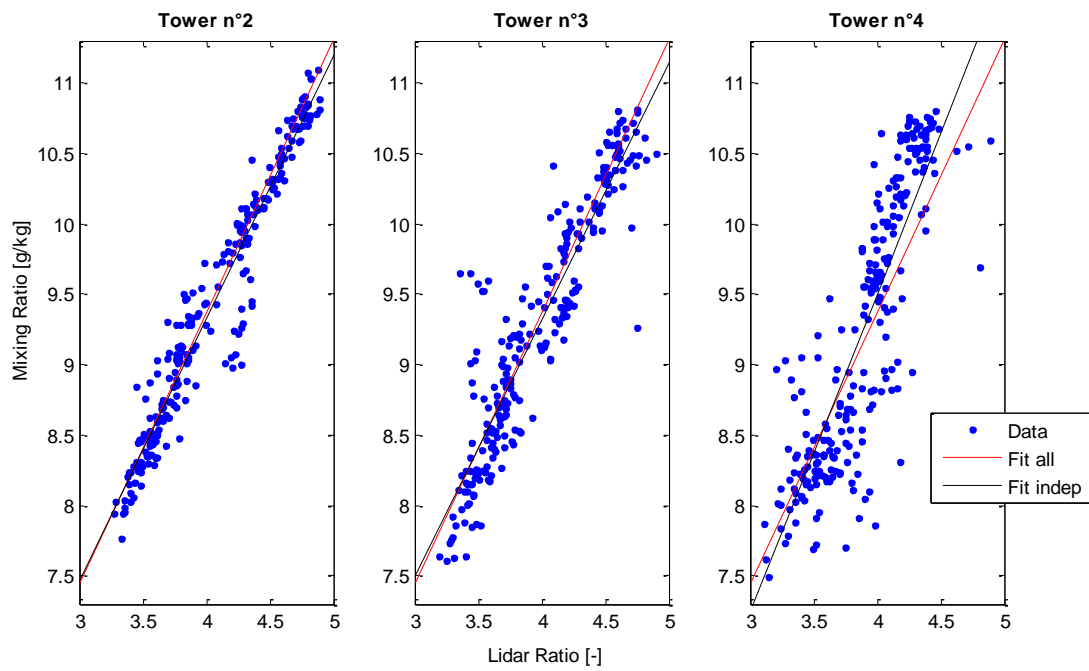


1

2 Figure 1 : (top panel) Aerial photograph of the lake and experimental setup looking  
 3 toward the west, and (bottom panel) side view schematic of the experiment showing  
 4 the path of the lidar beam (red dashed line) relative to the surface and instruments.  
 5 The vertical line of sight of the sodar is indicated by the dashed yellow line. The  
 6 white disks on the lake surface represent the hobo sensors used to measure the lake  
 7 surface temperature. Two scintillometers were deployed along the blue dashed lines  
 8 and a tethered balloon provided profiles of humidity and temperature (not used in the  
 9 present analysis).

10

1

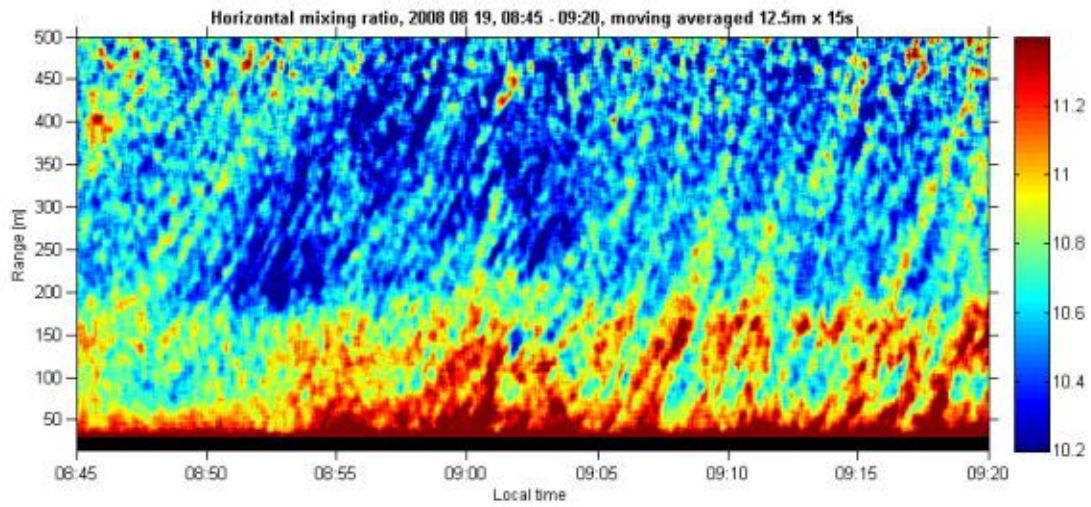


2

3 Figure 2: Lidar mixing ratio calibration curves at the three towers (60, 135 and 513  
4 meters) during TABLE-08.

5

1



2

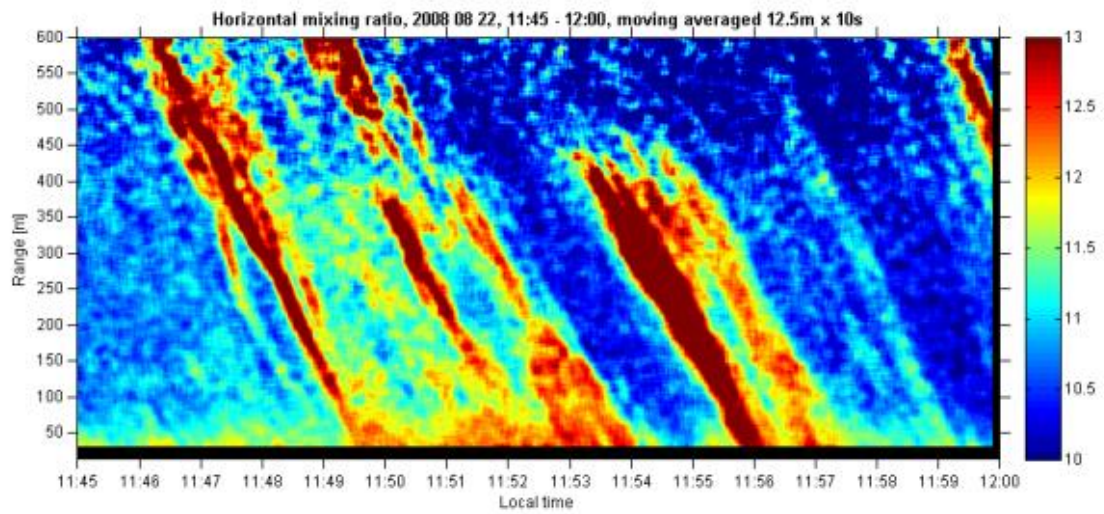
3 Figure 3: Contour plot of the evaluation of the mixing ratio during a horizontal scan  
4 (TABLE-08, 19 August 2008 08). The wind blows from the lidar (0 m) to the lake  
5 (150 -500 m), entraining water vapor from the grass field (0 – 150 m).

6

1

2

3



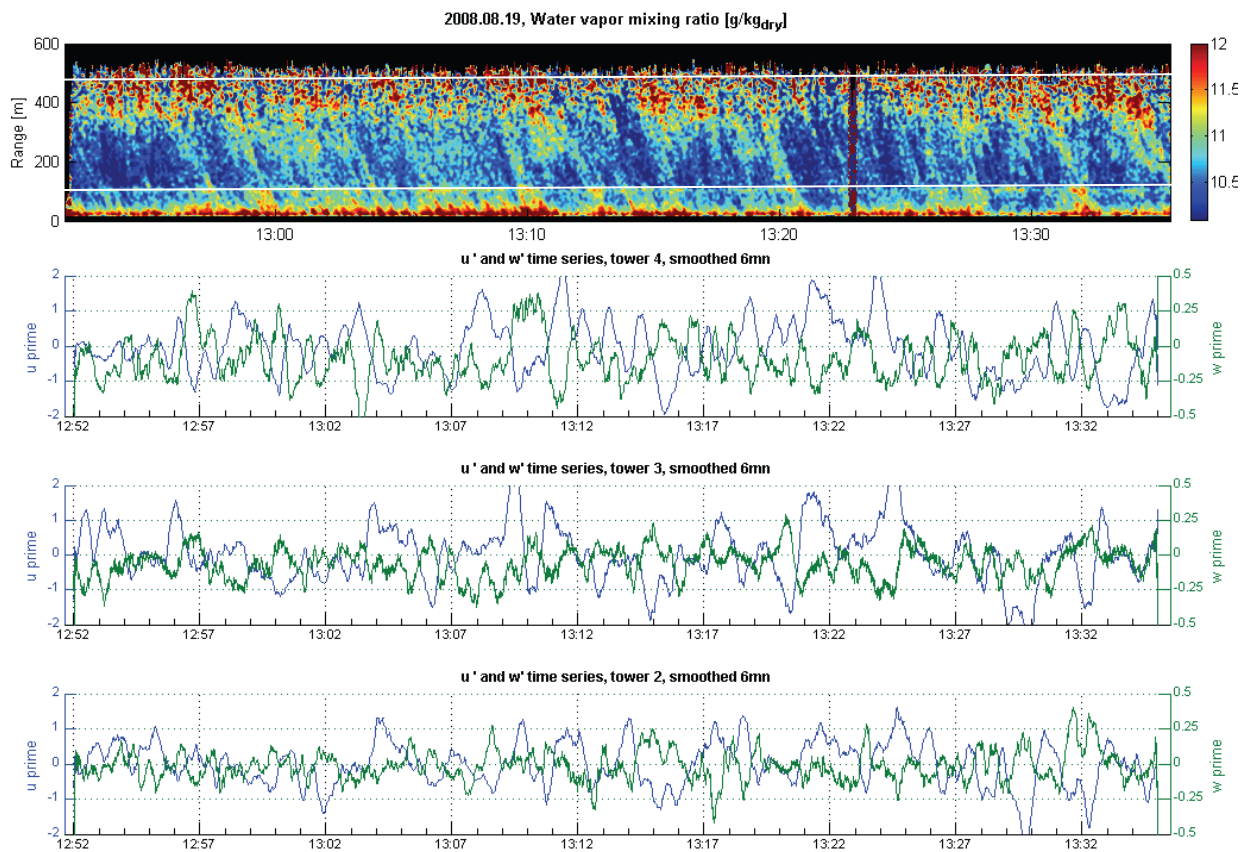
4

5 Figure 4: Horizontal lidar scan showing the mixing ratio evolution on 22 August  
6 2008. Large persistent flow features of humid air masses crossing the entire lidar  
7 observation range can be observed. In this figure the prevailing wind direction is  
8 towards the lidar (from 600m to 0 m).

9



1



2

3 Figure 5: time series of the fluctuating stream-wise and vertical velocity components  
 4 shown with the corresponding lidar humidity image. White lines on the upper panel  
 5 represent the positions of Towers 3 and 4 (122 m and 486 m respectively) at the edges  
 6 of the lake.

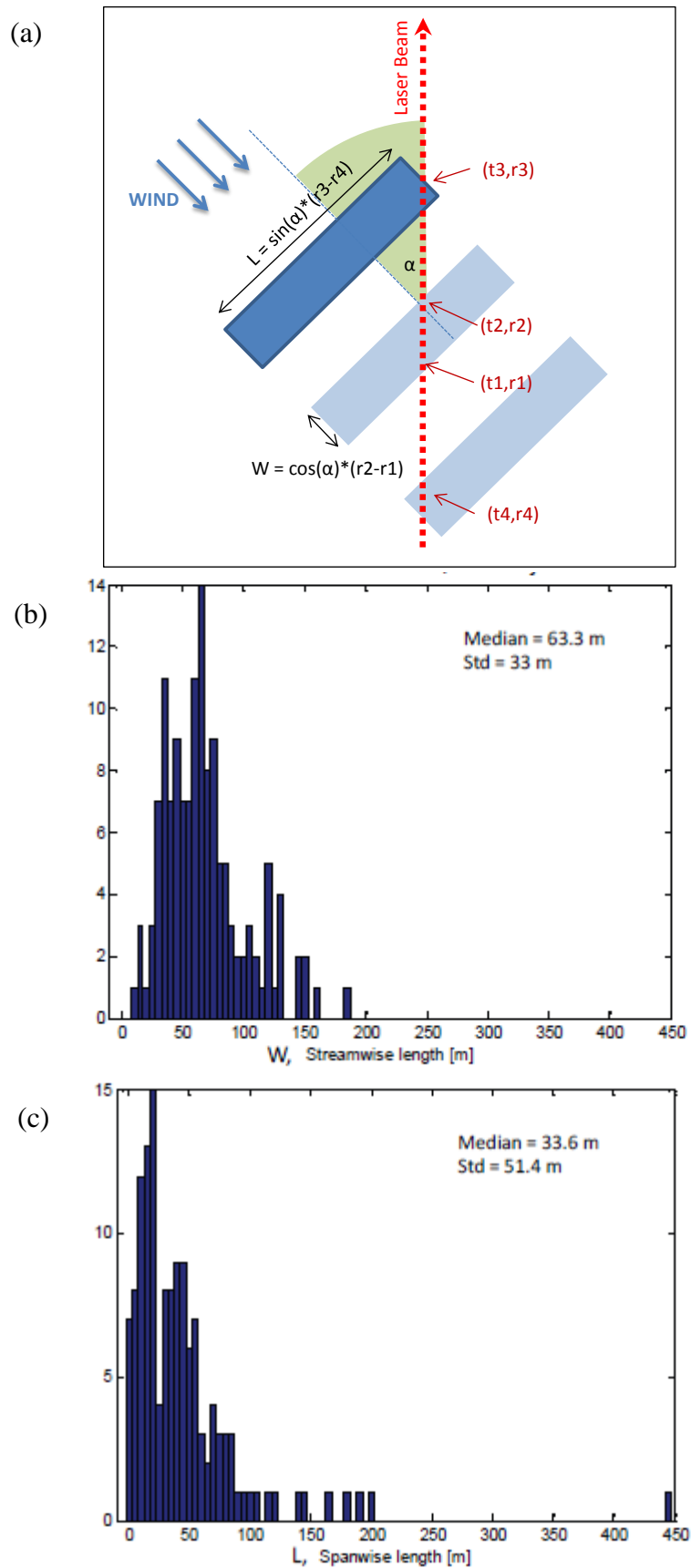
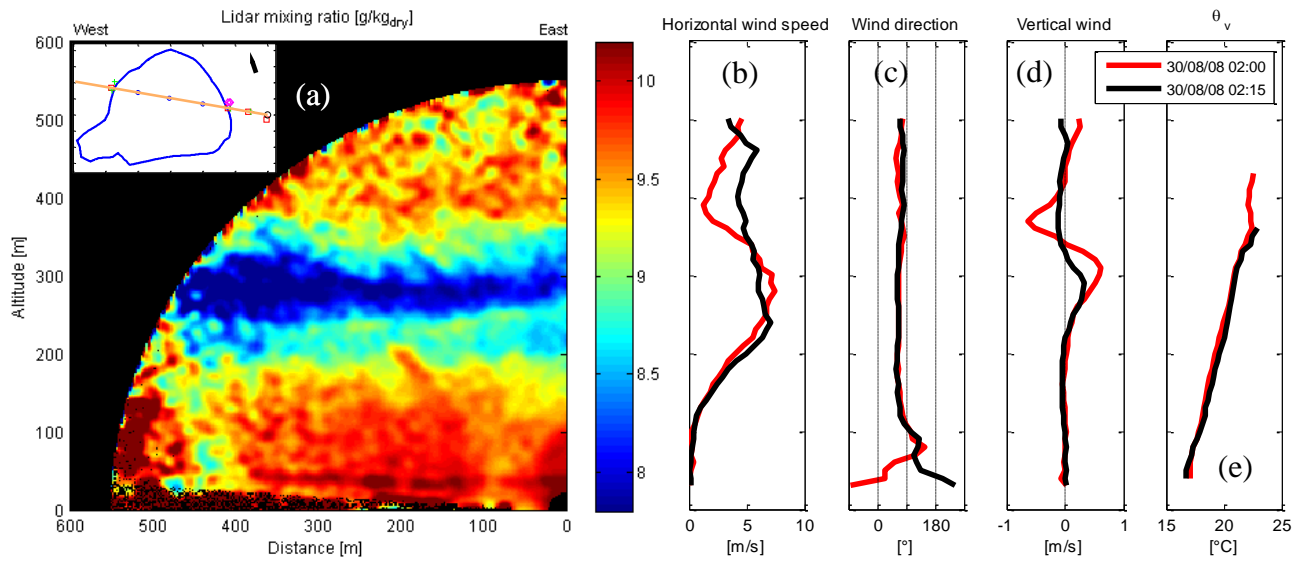


Figure 6: (a) Schematic of the coherent structure geometry analysis principle. (b) A histogram of the streamwise size of the coherent structures, and (c) a histogram of the cross-stream size of the structures



1

2



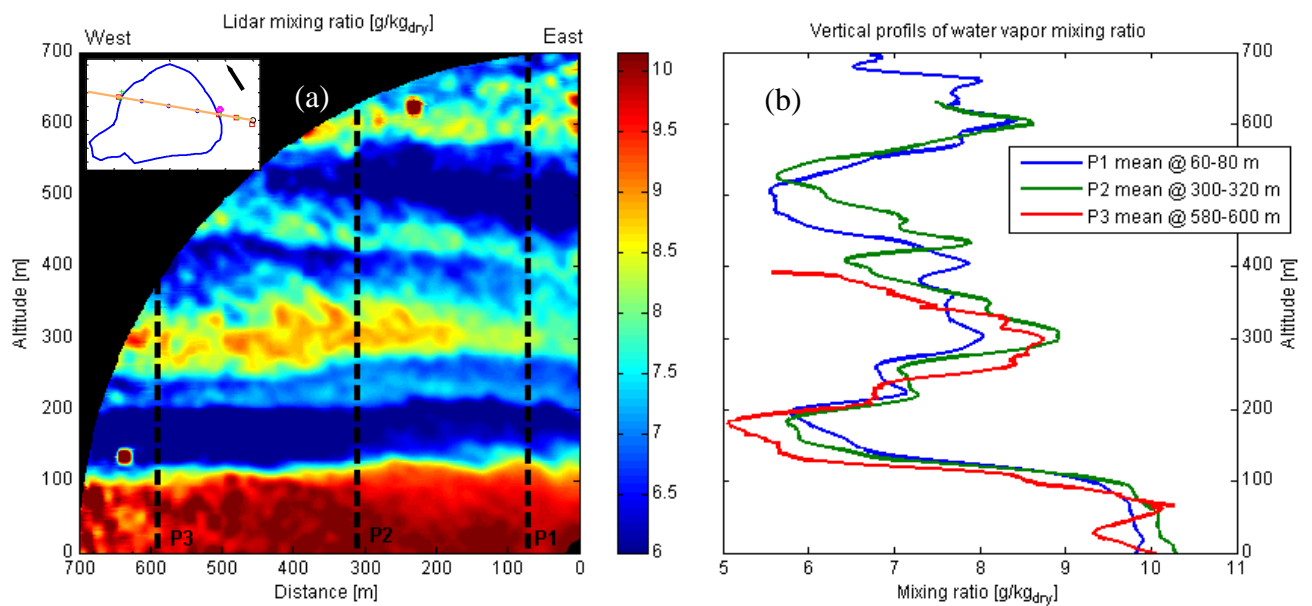
3

4 Figure 7: (a) Vertical lidar scan taken between 02:03 to 02:20 CET with profiles of  
 5 wind speed (b), wind direction (c), vertical wind (d) and virtual potential temperature  
 6 (e) Profiles were measured with the Sodar-Rass instrument at 2:00 CET (red line) and  
 7 2:15 CET (black line). The black points at the bottom part of the lidar scan in (a) are  
 8 due to fog scattering. The nocturnal jet at about 280 m produces a distinct layer of dry  
 9 air. At this time, the Obukhov length was 4.6 m measured at Tower 2 (height of  
 10 measurement 2.47 m). The vapor pressure deficit measured at Tower 2 was 0 hPa,  
 11 consistent with the formation of fog.

12

1

2

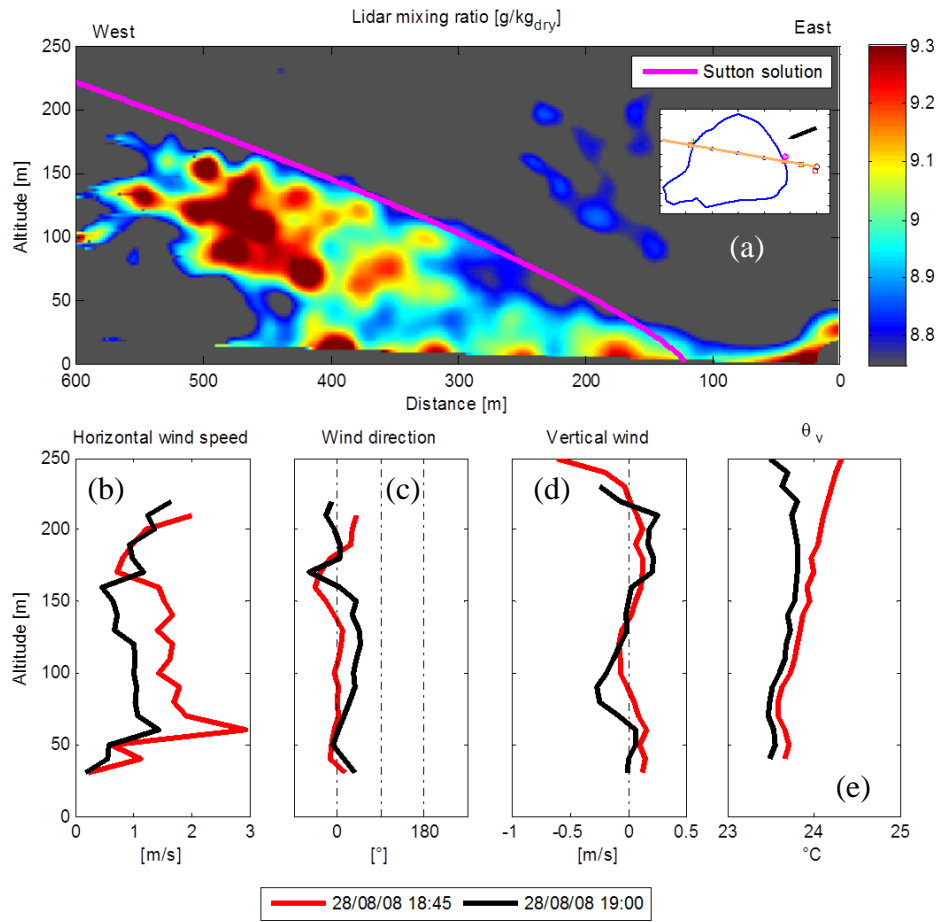


3

4 Figure 8: (a) Vertical lidar scan taken between 21:10 and 21:30 CET on the 29<sup>th</sup> of  
 5 august, and three extracted profiles (b). The profiles were extracted from the lidar  
 6 scan at the locations indicated by the vertical dashed lines. The 100 first meters of the  
 7 ABL exhibits large water vapor concentration where the internal boundary layer from  
 8 the lake is slightly visible. Numerous water vapor layers are visible above the lake. At  
 9 this time, the Obukhov length was 2.7 m measured at Tower 2 (height of  
 10 measurement 2.47 m). The vapor pressure deficit measured at Tower 2 was 2.7 hPa.

11

12



1

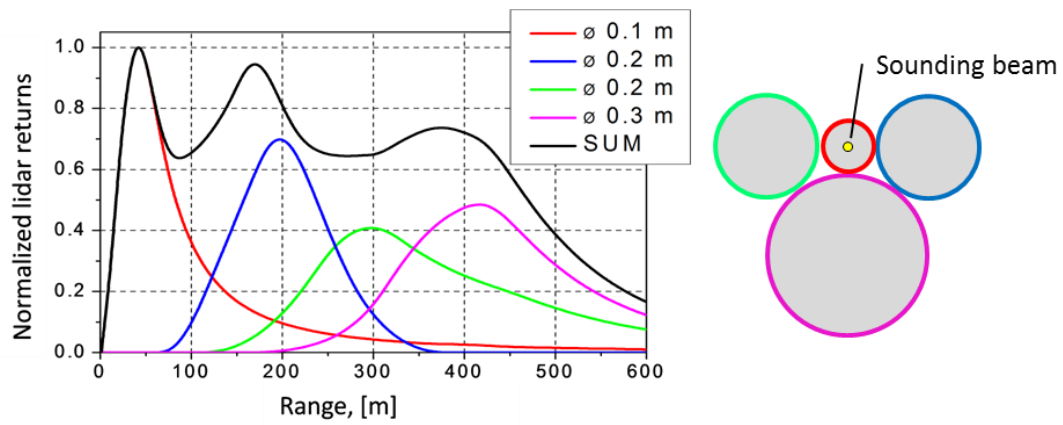
2 Figure 9: (a) Plot of water vapor mixing ratio from a vertical scan illustrating the  
 3 existence of a moist internal boundary layer. The lidar scan was taken between 18:31  
 4 and 18:53 CET on August 28<sup>th</sup> 2008. Profiles from the Sodar-Rass are presented of  
 5 wind speed (b), wind direction (c), vertical winds (d), and potential temperature (e).  
 6 The Sutton solution is shown in pink. At this time, the Obukhov length was -2.8 m  
 7 measured at Tower 2 (height of measurement 2.47 m). The vapor pressure deficit at  
 8 Tower 2 was 17 hPa.

9

10

11

1 **Figures from appendix**



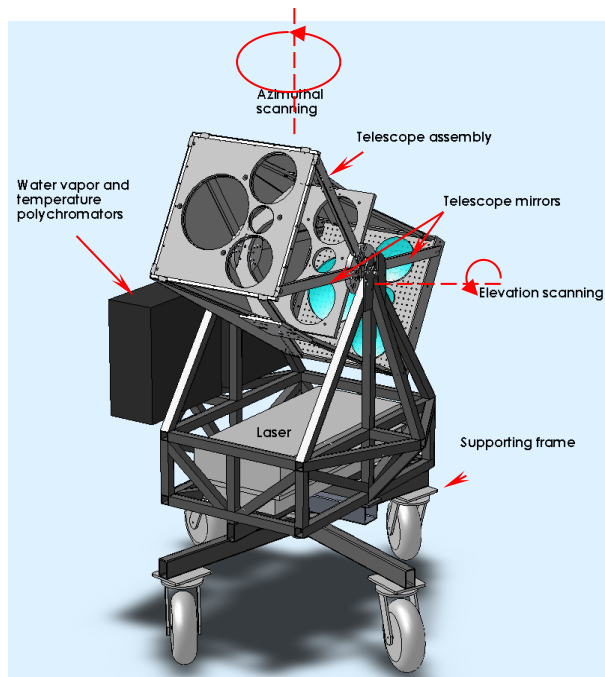
2

3 Figure A.1: (left) Individual and total normalized lidar return signal, and (right)  
 4 illustration of the four-telescope design with mirrors of diameters 0.1, 0.2, and 03 m.

5

1

2



3

4 Figure A.2: 3D projection of the EPFL Raman lidar.

5

6

1 Table 1: TABLE-08 Sensors summary

Intruments sites	Height [m]	Range [m]	Measured variables	Sensor type	Sampling rate	Accuracy
LIDAR		15-600	MR	Ro-vibrational Raman	1 s	±0.3 g/kg
			T	Pure-rotational Raman	1s	unknow
SODAR/RASS		30-400	u,v,w	MFAS Scintec	15 mn	±0.1, 0.1, 0.05 m/s
			Tv	RASS Scintec	15 mn	±0.2 °K
Balloon		0-200	P, alt	SW35	1-5 s	±0.5 hPa, ±0.5 m
			T dew, T	SW35 with SRS-C34	1-5 s	±0.1 °K, ±0.2°K
Tower 1	2.50		u,v,w, Tv	Ultrasonic anemometer	20 Hz	±1, 1, 0.5 mm/s, ± 0.002 °K
			q, CO2	Open-path analyser	20 Hz	± 0.26, ± 0.01 mmol/m3
			N2O, CH4, H2O, CO2	Quantum Cascade Laser	10 Hz	unknow
Tower 2	2.50		u,v,w, Tv	Ultrasonic anemometer	20 Hz	±1, 1, 0.5 mm/s, ± 0.002 °K
			q, CO2	Open-path analyser	20 Hz	± 0.26, ± 0.01 mmol/m3
			RH(2x), T(3x)	capacitive, Pt100, TC	5 s	±1 %, ±0.2°K, ±0.2°K
			P, T surf	P Transducer, IR gun	1 mn	±0.5 hPa, ±0.3 °K
			wdir, wspeed	Wind vane, cup	1 mn	±2°, ±0.1 m/s
			LW(up/dw)	Radiometers	1 mn	± 2%, ±3%
			G	thermopile	1 mn	±5%
Tower 3	4.34		u,v,w, Tv	Ultrasonic anemometer	20 Hz	±1, 1, 0.5 mm/s, ± 0.002 °K
			q, CO2	Open-path analyser	20 Hz	± 0.26, ± 0.01 mmol/m3
			RH, T	capacitive, Pt100	5 s	±1 %, ±0.2 °K
			H, Ct2	SLS	1-5 mn	unknow
			soil $\psi$ , Soil T, Soil $\theta$	ceramic, thermistor, dielectric	2 mn	±5kPa, ±1 °K, ±2%
Tower 4	7.07		u,v,w, Tv	Ultrasonic anemometer	20 Hz	±1, 1, 0.5 mm/s, ± 0.002 °K
			q, CO2	Open-path analyser	20 Hz	± 0.26, ± 0.01 mmol/m3
			RH, T	capacitive, Pt100	5 s	±1 %, ±0.2 °K
			P, T surf	P Transducer, IR gun	1 mn	±0.5 hPa, ±0.5 °K
			H, Ct2	Scintillometer	5 mn	unknow
			Rain	Rain gauge	2 mn	±10%
			Rn, wdir, wspeed	pyranometer, Anemometer	2 mn	±5%, ±7%, ±1m/s
			RH, T	capacitive, thermistor	2 mn	±3 %, ±0.5 °K
LAKE	0.00		water T	Thermistor	5s	±0.2 °K
	0.00		water T	Thermistor	5s	±0.2 °K
	0.00		water T(3x)	Thermistor	5s	±0.2 °K

2

3